

# Scanning PIV investigation of the laminar separation bubble on a SD7003 airfoil

Wei Zhang · Rainer Hain · Christian J. Kähler

Received: 20 November 2007 / Revised: 26 August 2008 / Accepted: 26 August 2008 / Published online: 23 September 2008  
© Springer-Verlag 2008

**Abstract** A laminar separation bubble occurs on the suction side of the SD7003 airfoil at an angle of attack  $\alpha = 4\text{--}8^\circ$  and a low Reynolds number less than 100,000, which brings about a significant adverse aerodynamic effect. The spatial and temporal structure of the laminar separation bubble was studied using the scanning PIV method at  $\alpha = 4^\circ$  and  $Re = 60,000$  and 20,000. Of particular interest are the dynamic vortex behavior in transition process and the subsequent vortex evolution in the turbulent boundary layer. The flow was continuously sampled in a stack of parallel illuminated planes from two orthogonal views with a frequency of hundreds Hz, and PIV cross-correlation was performed to obtain the 2D velocity field in each plane. Results of both the single-sliced and the volumetric

presentations of the laminar separation bubble reveal vortex shedding in transition near the reattachment region at  $Re = 60,000$ . In a relatively long distance vortices characterized by paired wall-normal vorticity packets retain their identities in the reattached turbulent boundary layer, though vortices interact through tearing, stretching and tilting. Compared with the restricted LSB at  $Re = 60,000$ , the flow at  $Re = 20,000$  presents an earlier separation and a significantly increased reversed flow region followed by “huge” vortical structures.

## 1 Introduction

A laminar separation is caused mostly by an adverse pressure gradient (APG) along a smooth aerodynamic surface. In the process, small disturbances are strongly amplified in the shear layer of the separated flow and the separated shear layer undergoes a rapid transition to turbulence. The turbulence reattaches to the surface due to a large momentum transport created and finally a closed bubble is formed in the time-averaged mean, which is termed the “laminar separation bubble (LSB)”.

LSB is a classic topic in fluid mechanics due to its importance in laminar-turbulence transition, which inevitably appears in many engineering applications ([2, 15], among others). Increasing interest in LSB is aroused by the development of micro air vehicles (MAVs), which normally operate in the Reynolds number range of 50,000–200,000 [26]. In this low-Re flow regime, LSBs bring about significant adverse aerodynamic effects, especially the augmentation of the pressure drag. In the extreme circumstance that the turbulence is not able to reattach to the rear part of the airfoil surface and a large separation area

---

W. Zhang · R. Hain · C. J. Kähler  
Institut für Strömungsmechanik,  
Technische Universität Braunschweig,  
Bienroder Weg 3, 38106 Braunschweig, Germany

*Present Address:*  
W. Zhang  
Department of Aerospace Engineering,  
Iowa State University, Ames, IA 50014, USA  
e-mail: weizhang@iastate.edu; weizhang@tu-bs.de

*Present Address:*  
R. Hain  
Deutsches Zentrum für Luft- und Raumfahrt e.V. (DLR),  
Institut für Aerodynamik und Strömungstechnik,  
Lilienthalplatz 7, 38108 Braunschweig, Germany  
e-mail: rainer.hain@dlr.de

*Present Address:*  
C. J. Kähler (✉)  
Institut für Strömungsmechanik und Aerodynamik,  
Universität der Bundeswehr München,  
Werner-Heisenberg-Weg 39, 85577 Neubiberg, Germany  
e-mail: christian.kaehler@unibw.de

occurs, there will be a sudden loss of lift and a strong increase of drag with considerable hysteresis effects. Therefore, it is essential to understand the underlying physics involved in the LSB prior to controlling it.

The mean flow characteristics of the LSB have been studied with various theoretical, numerical and experimental approaches. The early work of Gaster [10] is a comprehensive study of laminar separation bubbles on a flat plate over a wide range of Reynolds numbers and pressure distributions. He found that the length of the separation bubble suddenly increased when the APG and/or the Reynolds number exceeded certain critical values, which was called “bubble bursting”. Also, he proposed an improved scaling for predicting the formation of long or short bubbles. This work contributes to building an empirical correlation between global quantities of the bubble and boundary layer properties at the separation point. Horton [17] presented the mean flow structure of a 2D LSB, which is widely cited by following research on this topic. More recently, Ol et al. [24] employed standard PIV methods to determine the mean flow structure and the Reynolds shear stresses of the LSB on the SD7003 airfoil in three different flow facilities.

It has been noticed that the LSB is inherently unstable, sensitive to the ambient fluid environment, such as the turbulence intensity of free-stream, acoustic waves, pressure gradient, surface roughness, external turbulence and other disturbance. Unsteadiness of the separation bubble was investigated by Pauley et al. [25]. They studied the boundary layer separation on a channel wall experiencing an artificial APG made by initiating suction through a port in the ceiling. Basically this is a numerical experiment comparable to Gaster’s measurements. It was found that a strong APG resulted in periodic vortex shedding from the bubble. More interestingly, Pauley et al. [25] suggested that ‘bursting’ of a short separation bubble reported by [10] was the time-averaged result of vortex shedding. In addition, Alam and Sandham [2] simulated a short separation bubble by Direct Numerical Simulation (DNS). Different from 2D simulations by Pauley et al. [25], this 3D computation leads to the finding that the transition was characterized by  $\Lambda$ -vortex-induced breakdown. Windte et al. [31] calculated transitional flow past the SD7003 airfoil using a Reynolds-averaged Navier-Stokes (RANS) method. In particular, a newly proposed  $e^N$ -scheme in combination with a linear stability solver was employed to predict the transition onset. Yuan et al. [33] reported computation of the flow past this airfoil by means of the state-of-the-art Large eddy simulation (LES) as well as the RANS method, and compared their results with experimental observation. Eisenbach and Friedrich [11] also applied LES to study flow separation of an airfoil at  $Re = 100,000$  but at a high angle of attack ( $18^\circ$ ). More recently, the DNS results of laminar separation bubbles

on a NACA-0012 airfoil at  $Re = 50,000$  and  $\alpha = 5^\circ$  were presented by Jones et al. [19]. On the one hand, these work shows that the computational methods are very promising to facilitating understanding of the flow physics, and as well can serve as practical tools for aerodynamic analysis. On the other hand, it can be inferred that the complicated interdependence of the flow characteristics at low Reynolds number, such as laminar separation, transition, and turbulent reattachment are obstacles to the computational model development. In this sense, reliable experimental data are very useful for validating new models and providing a data base for comparison with computational results.

Compared with the numerical studies of the LSB, there are few experimental results probably due to the complicated flow nature and drawbacks of the available measurement techniques. Watmuff [30] used a flying hot wire system to track evolution of an introduced disturbance into the reattachment region and the fully turbulent boundary layer. The wave packet is found to be associated with Kelvin-Helmholtz instability, and further stream-wise development leads to the formation of 3D roll-ups, and finally a group of large-scale vortex loops in the vicinity of the reattachment. With the help of PIV-related techniques, Hain and Kähler [13] discussed the Tollmien-Schlichting instability (T-S-waves) and its relationship with the vertical oscillation of the LSB formed on the suction side of the SD7003 airfoil. Hu and Yang [18] mapped Kelvin-Helmholtz (K-H) vortex structures of LSB on a NASA low-speed GA (W)-1 airfoil at the chord Reynolds number of 70,000 at various angles of attack.

A 3D measurement technique is desirable because of the complicated 3D vortex structure in the vicinity of the reattachment region of the LSB. The scanning PIV technique employed in the present study is a quasi-3D measurement technique, extended from the standard PIV methods. In principle, it combines classical PIV technique with volume scanning using a scanning light-sheet. Therefore this technique allows capture of particle images in a stack of parallel illuminated planes to obtain a set of “cuts” of the studied flow. Furthermore, it enables the volumetric reconstruction of the instantaneous scalar distribution, vorticity for example, as demonstrated by Brücker and Althaus [3] on the study of vortex breakdown. The scanning movements of light sheets can be generated by oscillating mirrors, polygon mirrors, rotating prism scanners and drum scanners. In particular, oscillating mirrors are typically commercial galvanometer-driven units with linear response and a high roll-off frequency in the hundreds or even thousands (to date) depending on the sweeping angle. General description of various scanning-PIV-related techniques can be referred to [22].

Practical examples of the scanning PIV application are provided by Brücker and his coworkers [3, 4, 5, 6] who

carried out a range of volumetric measurements of various flows, such as vortex breakdown, the unsteady flow behind a starting short circular cylinder, the near wake of a spherical cap and the flow in a T-junction. Some of the work performed 2D PIV on discrete parallel planes and reconstructed 3D flow information in planes with different orientations. Other work extracted three velocity components by measuring the out-of-plane component with stereoscopic imaging or integrating the continuity equation. However, these applications of scanning PIV techniques often suffered from the low energy of the available light source (e.g., CW Argon ion laser), low sampling rate of the image devices (video camera) and low frequency of the oscillating mirrors. As a result, turbulent flows at relatively high Reynolds numbers cannot be resolved sufficiently.

The state-of-the-art scanning PIV techniques are facilitated by the development of the high frequency diode-pumped solid state lasers and high frame rate CMOS cameras with mega pixel resolution. Thanks to these new technologies, Hori and Sakakibara [16] built a scanning stereo PIV system which was capable of measuring the 3D-3C velocity distribution in a measurement volume of  $100 \times 100 \times 100 \text{ mm}^3$  of a fully developed turbulent jet. The light source was a pulsed Nd:YLF laser with 20 mJ/pulse at 2,000 Hz. Two CMOS cameras of  $1,024 \times 1,024$  pixels at 2,000 fps were used to capture the particle images. Scanning light sheets were achieved with a fast optical scanner. Also, the scanning PIV technique was applied to study the LSB on the SD7003 airfoil by [7–9]. A unique light sheet illumination system composed of ten adjustable laser diodes with a power of 50 W in continuous mode at a wavelength of 805 nm was employed. Note that this illumination system is quite different to the pulsed laser widely used in PIV methods. Particle images were recorded with a high speed CMOS camera at frame rates of 308 and 922 Hz. They concerned spatial and temporal evolution of the vortex dynamics at the downstream end of the separation bubble at the angle of attack  $\alpha = 4\text{--}8^\circ$  and  $Re = 20,000$ . A complicated vortex system emerging from this region of interest is revealed, such as halfmoon- or C-shape vortices and screwdriver vortices.

Despite much effort put in this topic, the description of the LSB, especially the physical mechanism of the transition is far from complete due to the elusive nature of the LSB. In the present work emphasis will be put on the dynamic vortex behavior of the LSB on the suction side of the SD7003 airfoil at  $Re = 60,000$  studied by means of the scanning PIV technique. The SD7003 airfoil is designed for model planes operating in the Reynolds number range of 50,000–200,000. A separation bubble appears in the angle of attack range of  $\alpha = 4\text{--}8^\circ$  as the Reynolds number is below 100,000. The LSB at the angle of attack  $\alpha = 4^\circ$  and  $Re = 60,000$  is most interesting from the point of view

of practical significance. Detailed measurements were made to examine the LSB on this airfoil at  $Re = 20,000$  [7–9]. As the airfoil is not optimized for this Reynolds number the flow phenomenon in this case is expected to be different from that at  $Re = 60,000$ .

The remainder of this paper is organized as follows: Firstly, detailed experimental apparatus and measurement conditions are documented in Sect. 2. Afterwards the evolution of spatial structures of the LSB are shown and discussed from different views, leading to a comprehensive understanding of the LSB behaviors in Sect. 3. And finally Sect. 4 contains a summary and concluding remarks.

## 2 Experimental apparatus and methods

### 2.1 Flow facility and scaled airfoil model

Experiments were performed in a Göttingen type water channel with a test section of  $1.25 \text{ m}^L \times 0.25 \text{ m}^W \times 0.33 \text{ m}^H$  in the Institute of Fluid Mechanics at Braunschweig University of Technology. To avoid the free surface influence, a metal plate was placed from the water channel top for all measurements. This water channel has a turbulence level of approximately 0.28% as the free-stream speed is 0.3 m/s without any filtering.

A transparent SD7003 airfoil was mounted upside down between the side walls and parallel to the free-stream direction, exposing the suction side to the optical access from bottom (see Fig. 1). Herein the laminar separation bubble on the SD7003 airfoil was measured at an angle of attack  $\alpha = 4^\circ$  and  $Re = 60,000$  and 20,000 defined by the airfoil chord length of  $c = 200 \text{ mm}$  and the free-stream velocity  $U_0$ . The free-stream velocity was adjusted to meet the requirement of the Reynolds number based on the water temperature measured prior to each measurement case. Measurements were carried out from two orthogonal views: the former observation in the stream-wise wall-normal planes from side, and the latter observation in the airfoil surface-parallel planes from bottom. The schematic diagram of the measurement sections in a Cartesian coordinate system is shown in Fig. 1.

### 2.2 Scanning light sheet system

A 20 W diode-pumped dual-head Nd:Yag laser (Lee laser) was employed as the light source. Each laser can work over a range of pulsing frequencies, with the energy per pulse decreasing as the frequency increases. Specifically, the output energy is 20 mJ/pulse at 1,000 Hz and 10 mJ/pulse at 2,000 Hz. The laser was operated at 1,000 Hz, taking into account that the laser power must be high enough to illuminate the seeding particles without damaging the oscillating mirror.

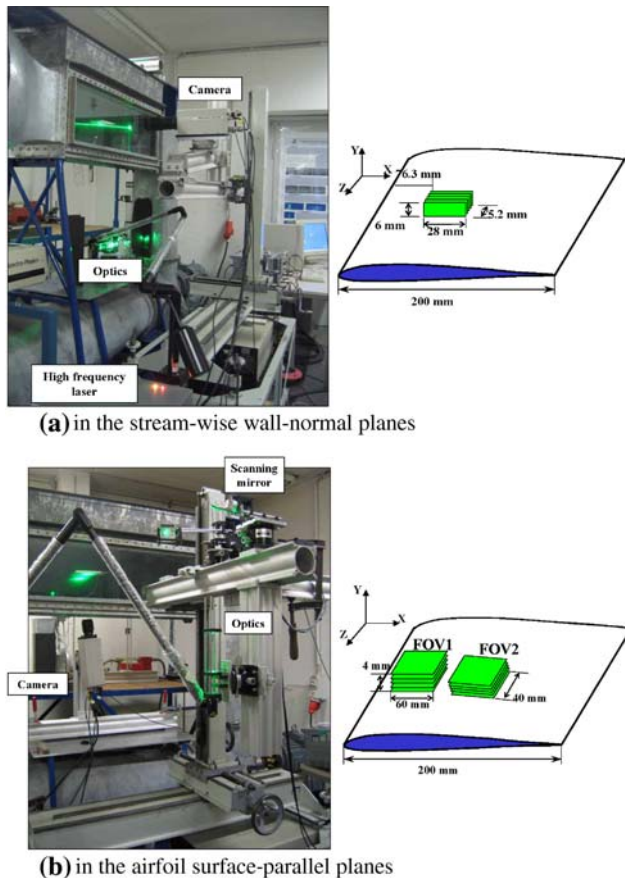


**Fig. 1** Experimental setup for the scanning PIV measurements from two orthogonal views

For generating scanning light sheets, an oscillating mirror and a long focal length cylindrical lens were applied in addition to the combinations of optics serving to expand the laser beam. In this study two optical setups were built for the measurements in the stream-wise wall-normal planes and those parallel to the airfoil surface, as mentioned in Sect. 2.1. In the first configuration shown in Fig. 1a, two spherical lenses ( $f = -50$  mm and  $f = +150$  mm) and a cylindrical lens ( $f = 200$  mm) were used to form the light sheet with a desirable width and thickness. Then the light sheet was scanned by a flat 8 mm mirror mounted on an optical scanner (VM1000, GSI Lumonics), which was accurately controlled by the SC2000 program (GSI Lumonics). A rectangular cylindrical lens ( $f = +300$  mm), whose focal line was positioned in the oscillating axis, ensured the scanning light sheets were parallel to each other. A reflection mirror was put 300 mm behind the airfoil tail and reflected scanning light sheets to the desired measurement position. Light sheets were adjusted to be approximately 8 mm high at  $Re = 60,000$  and up to 10.5 mm at  $Re = 20,000$  in the stream-wise wall-normal direction to cover the region of interest with given laser power capability. As can be seen in the

following results, the light sheet breadth was sufficient to cover the area of interest at  $Re = 60,000$ , but not at  $Re = 20,000$ . For the second configuration, the optics applied to form light sheets are similar, except that two spherical lenses with  $f = -50$  mm and  $f = +100$  mm were included, see Fig. 1b.

To determine the dimension of the scanning volume along with each of the light sheet thickness, a metal scale inclined by  $19^\circ$  with respect to the light sheet incidence was put in the measurement area so that the illumination by the multiple light-sheets could be directly recorded with the camera. Figure 2 shows the light sheet intensity distribution on the scale surface for the measurement in the stream-wise wall-normal planes. The light sheet thickness  $\delta$  in the measured area was estimated to be 0.2 mm and the interval between adjacent light sheets was  $\Delta z = 1.3$  mm. Therefore the entire scanning volume was  $Z = 5.2$  mm measured from each light sheet center for the first optical configuration. In the same way the entire scanning volume was estimated to be  $Z = 4.0$  mm with  $\Delta z = 1.0$  mm spacing for the measurements in the surface-parallel planes. Moreover, by observing the image sequence the position repeatability of the multiple light sheets was found to be satisfactory for both optics configurations.

### 2.3 Scanning mode and synchronization

Determination of the scanning mode depends on the time scales of the investigated flow. Firstly, the duration of the complete volume scan  $T_{\text{step}}$  is required to be less than half of the flow time scale according to the Nyquist criterion. Secondly, the time between two correlated PIV images  $T_{\text{piv}}$ , must be suitable to ensure that the seeding particles remain within the defined interrogation windows. Two typical scanning modes are shown in Fig. 3. The upper graph



**Fig. 2** Intensity distribution of five scanning light sheets on a metal scale with an inclined angle of  $19^\circ$

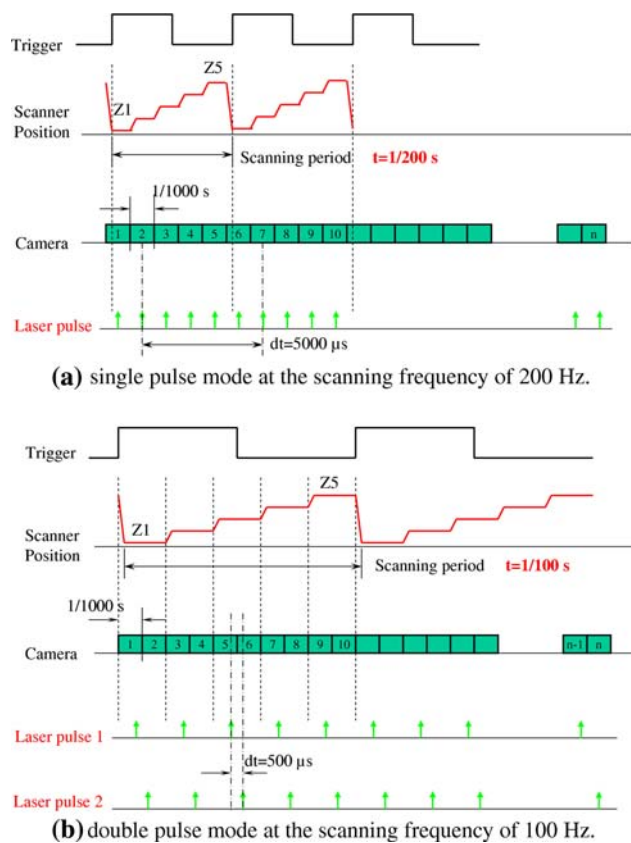


**Fig. 3** Timing diagram of the PIV measurements for two typical scanning modes

represents the single frame mode, in which only one particle image is captured in each scanned plane and the PIV cross-correlation is carried out with two images recorded in the same plane but neighboring scanning cycles. For example, the correlated images in Fig. 3a are frame 1 and frame 6, frame 2 and frame 7 and so on, given that each scanning cycle consists of 5 planes. Though only one laser pulse is needed, the drawback inherently with this mode is that the flow velocity can be measured with PIV cross-correlation is limited by the amount of scanning planes and  $T_{\text{step}}$ . Therefore, compromise must be made among the tested flow velocity, amount of scanning planes and  $T_{\text{step}}$ . Burgmann et al. [8] commented that the single frame mode limited either the amounts of the scanning planes or the maximum flow speed that could be studied. Accordingly, they were able to successfully measure the LSB at  $Re = 20,000$  using their scanning PIV system but unfortunately not at higher Reynolds numbers, for instance,  $Re = 60,000$ . Alternatively, the double frame mode allows a pair of particle images to be captured with frame-straddling in each scanned plane, as can be seen in Fig. 3b. Since the time interval between the paired images  $T_{\text{piv}}$  could be adjusted flexibly, relatively high velocity flow can be studied. But in this case, two laser pulses are needed and the  $T_{\text{step}}$  is doubled.

The high speed camera with a frame rate of 1,000 Hz serves as the master to synchronize the scanning PIV system. A pulse generator was applied to trigger the optical scanner to start a scanning cycle once it received a signal from the camera. The laser was also triggered by the camera to give a pulse at each scanned plane. Additionally, an oscilloscope was included to monitor the signal sequence and to modify the phase shift between the camera frame and scanning mirror position feedback signal conveniently. In this study, the oscillating mirror swept five steps at 200 Hz with the single frame mode for the measurements at  $Re = 20,000$  and 100 Hz with the double pulse mode at  $Re = 60,000$ , respectively. The corresponding duration of the complete volume scan  $T_{\text{step}}$  is 1/200 and 1/100 s. And the separation time between cross-correlated images is 5,000 and 500  $\mu\text{s}$ .

## 2.4 Image acquisition

Hollow glass beads with a median diameter of 10  $\mu\text{m}$  were employed as the seeding particles. The particle images were recorded by a high-speed CMOS camera (Redlake) with the single pixel size of 12  $\mu\text{m}$ . Herein the full spatial resolution of  $1,504 \times 1,128$  pixels at a frame rate of 1,000 was determined in order to make use of illumination as much as possible. For the measurements in the stream-wise wall-normal planes, the field of view (FOV) of approximately 30 mm  $\times$  10 mm was obtained by a 180 mm long focal lens. And the camera was positioned to align the CMOS sensor parallel to the local airfoil surface contour (see Fig. 1), to avoid the PIV evaluation difficulty adjacent to inclined surfaces by using commercial software. For the measurements in the airfoil surface-parallel planes, a 60 mm micro lens was involved to get a FOV around 60 mm by 40 mm. In total 2,530 single frames with the single frame mode and 1,265 image pairs with the double frame mode were acquired at each FOV, lasting for 2.53 s and occupying 4G memory.

It should be noted that illumination is a significant determinant of the performance of a volume imaging system. The output energy of diode-pumped lasers working at high repetition rates, 1,000 Hz for instance, is typically only 10–20% of the laser energy normally applied in standard PIV measurements. The depth of field is estimated by  $\delta z = 4(1 + M^{-1})^2(F\#)^2\lambda$ , where  $M$  is the magnification factor of the lens,  $F\#$  is the  $F$  number of the lens and  $\lambda$  the wavelength of the light source. With the fixed wavelength of the light  $\lambda$ , if a relatively high magnification  $M$  is used to achieve a high spatial resolution, a large  $F\#$  will be needed to achieve the required depth of field, indicating that little light will enter the image sensor. In this case, the light intensity is so low that particle images cannot be identified from the background even with high quality laser and

cameras. On the other hand, if a small  $F\#$  is decided to get sufficient light intensity given the same depth of field, a small  $M$  will be required, which means a low spatial resolution of the studied flow. Compromise between achieving sufficient illumination and enough sharp particle images leads to the selection of  $F\#$  of 5.6, though blurred particle images beyond the depth of field are hard to avoid in this case. Since a high magnification factor is desirable, especially for the measurements in the stream-wise wall-normal planes, this problem is more critical. Figure 4 compared the particle images in a  $128 \times 128$  pixels region, cropped from the raw images obtained in three planes of a scanning volume. The particle image diameter is on average 6–7 pixels in the first and the last plane, two or three times the particle diameter in the central plane (2–3 pixels) where the camera is focusing. Evidently the depth of field is not capable of covering the entire scanning volume. In this case the PIV image processing becomes more difficult because the Gaussian peak fit does not work very well for blurred particle images, reduced image contrast and apparently low particle density.

Furthermore, the magnification factor varies from plane to plane through the scanning volume. To check this effect, a home-made calibration target with 5 mm spacing grid was recorded at each measured plane. As seen from Table 1, the magnification factor of the images differs approximately in a linear way throughout the scanning volume, consistent with the linear response of the oscillating mirror. The maximum relative difference in the magnification factor between the first and the last planes was 0.3% and 0.8% for the two optics configurations. In this case, the data was corrected by applying a scale factor to consider magnification factor variation in the parallel scanned planes.

## 2.5 Data processing

The evaluation of the particle images was performed in each plane using Davis 7.1, with a second order multi-grid, multi-pass method and image deformation. The interrogation window size for the final pass was  $32 \times 32$  pixels with

**Fig. 4** Cropped particle images of a scanning volume in a  $128 \times 128$  pixels region in the stream-wise wall-normal planes

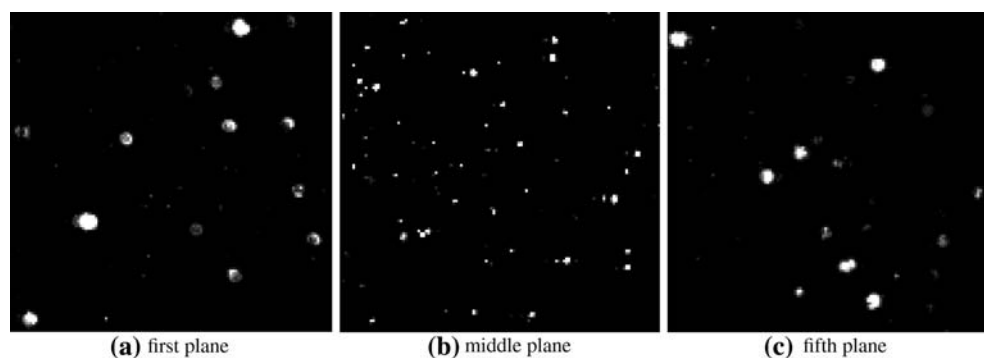


**Table 1** Magnification factor variation in a scanning volume

Plane	Distance in mm	Distance in pixel	Magnification factor	Maximum difference (%)
Stream-wise wall-normal planes				
1		1314.5	0.6310	
3	25	1316.5	0.6319	0.3
5		1318.6	0.6329	
Airfoil surface-parallel planes				
1		878.4	0.301	
3	35	874.8	0.300	0.8
5		871.2	0.2987	

50% overlapping. Table 2 summarizes the resulting spatial resolution and vector numbers for each measurement case. It is interesting to find that the amounts of spurious vectors in all scanned planes do not show much difference using the same final-pass interrogation window size. As far as the Q-factor of the vector field in the five scanned planes is concerned, which represents the ratio of signal-to-noise peaks in the correlation map, it is 2.5–2.7 in the central plane but drops to 1.9–2.4 in the extreme-near and extreme-far scanned planes. Overall, the range of Q-factor in all scanned planes indicates strong correlations. Elsinga et al. [12] studied the effect of the particle image blur on the correlation map and velocity measurement in PIV, and revealed that the correlation map was still symmetrical and no bias of peak identification was expected when particle images were blurred by the same amount in both PIV recordings. In the present study, the particle image blur is generally uniform in the same scanned plane, in which a pair of PIV recordings is cross-correlated. Therefore, we would not expect a large measurement uncertainty to be induced by the particle image blur itself and thus bias in the flow statistics.

From the 2D PIV data, either velocity or scalar fields in a series of parallel planes can be re-sampled to generate data fields in any sectional plane. In this vein, interpolation within the data volume is feasible. Furthermore volumetric reconstruction of the 2D data can be performed, and the iso-

**Table 2** Evaluation parameters for measurement cases

Measurement cases	Scanning volume (mm <sup>3</sup> )	Spatial resolution (mm)	Magnification factor	Vector number
Stream-wise wall-normal planes	28.3 × 6.5 × 5.2	0.59	0.632 ± 0.001	94 × 22 × 5
Airfoil surface-parallel planes	61.5 × 45.6 × 4.0	1.30	0.300 ± 0.001	94 × 70 × 5

surfaces of scalars can be examined to reveal the vortex evolution in detail. However, it is important to note that particle images in the individual planes of a scanning volume are not captured simultaneously. If there is convection in the flow, the flow pattern also moves between each scanned plane. Whether this convection effect is strong or not depends on the duration of an entire volume scanning cycle ( $T_{\text{step}}$ ) and the appropriate time scale of the investigated flow (local or mean velocity). In principle, the flow field should be corrected by taking into account local convection velocity of individual flow structures in every scanned plane. However, this is difficult since how to doubtlessly identify each flow structure is still an open question. Delo and Smits [22] corrected their data, compensating the convection effect by offsetting the velocity field in the stream-wise direction with the mean velocity field and the time delay during stack acquisition. This correction resulted in a skewed image volume. For the measurement cases at two Reynolds numbers, no doubt that the convection effect will be more noticeable at  $Re = 60,000$  than that at  $Re = 20,000$ . Now we consider the former case. As will be shown in the following section, the most interesting region is the separation bubble constricted in the near wall region, not the outer layer. It is reasonable to assume that the maximum convection velocity is comparable to the local stream-wise velocity, less than the free-stream velocity  $U_0$ . The ratio of the convection velocity of the flow structure and the scanning speed can be used to assess the effect [16]. The scanning speed is  $V_s = n \times \Delta z / T_{\text{step}} = 5 \times 1 \text{ mm} / 0.01 \text{ s} = 500 \text{ mm/s}$ . Hence the ratio is  $U_0 / V_s = 0.27 / 5 = 0.054$ , which is considered not to severely distort the topology of the instantaneous vortical structures.

### 3 Results and discussion

#### 3.1 Flow structures of LSB at $Re = 60,000$

##### 3.1.1 Mean flow field in the single stream-wise wall-normal plane

The mean velocity field and normalized stream-wise velocity magnitude contours in a single stream-wise wall-normal plane are shown in Fig. 5a and b. The FOV covers  $x = 76.3$  to  $104.5 \text{ mm}$  ( $x/c = 0.382$ – $0.523$ ) in the stream-

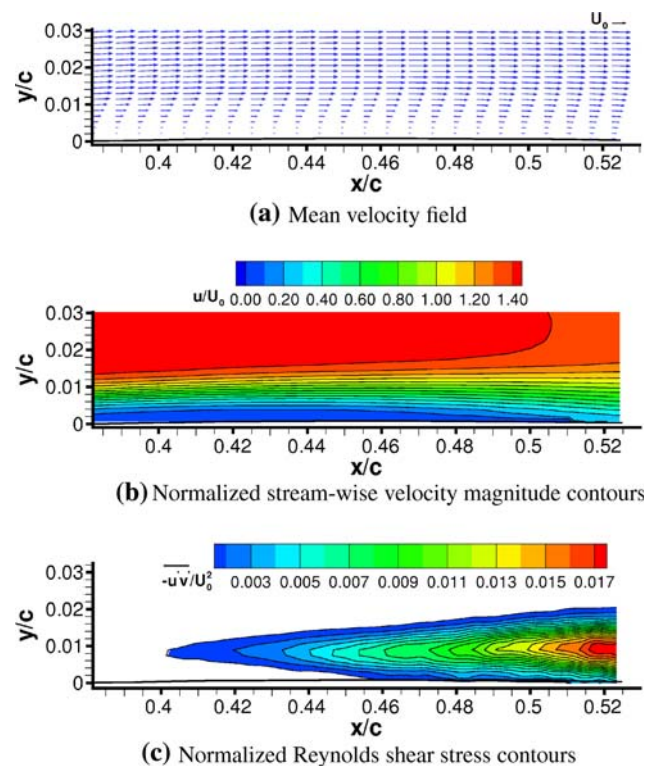


**Fig. 5** Mean flow field and the normalized Reynolds shear stress contours ( $-\overline{u'v'}/U_0^2 > 0.001$ ) at  $Re = 60,000$ . The FOV covers  $x/c = 0.382$ – $0.523$ , the transition onset is at  $x/c = 0.40$  and the reattachment point is at  $x/c = 0.51$ . The airfoil surface is outlined with the coordinate of  $y = 0$  at  $x/c = 0.382$

wise direction. A thin low-velocity fluid zone develops underneath the main portion of the boundary layer, but the entire boundary layer remains attached. This is the “dead fluid region” termed by [17]. The separation point can not be seen due to the small FOV.

The transition location was determined at the position where the normalized Reynolds shear stress reaches 0.1% [24, 33]. As presented in Fig. 5c, the contours of the normalized Reynolds shear stress display a typical wedge shape. The value undergoes a distinct rise in the stream-wise direction. Here the transition occurs at approximately  $x/c = 0.40$ , which is upstream compared with  $x/c = 0.57$ ,  $0.53$  and  $0.47$  reported in [24]. It is known that the laminar-turbulent transition is caused by a series of instability development in the laminar boundary layer. The turbulence intensity is around 0.28% for the free-stream of 0.3 m/s in

this water channel, higher than that in the low turbulence wind tunnel ( $T_u = 0.1\%$ ), the water channel ( $T_u \approx 0.1\%$ ) and the tow tank ( $T_u \approx 0$ ) in [24]. Therefore the turbulence intensity of the free-stream is attributed to work as the main disturbance to trigger the early transition. The reattachment point is estimated to be  $x/c = 0.51$ , also earlier than those in [24]. As will be seen in the following sections, this measurement domain is suitable to observe the laminar-turbulence transition and vortical structures in the vicinity of the reattachment.

### 3.1.2 Vortex shedding

Figure 6 shows the streamline distribution based on the instantaneous velocity field subtracting 0.6 times free-stream velocity ( $u - 0.6U_0$ ,  $v$ ) in the same single stream-wise wall-normal plane as in Fig. 5. In order to identify the vortical structures embedded in the velocity field, a range of translation velocities were tested, among which  $0.6U_0$  is found to be good at presenting the result. Though this value

may not be the exact vortex translation velocity, it still serves to visualize the vortices [1]. Color coded are the span-wise vorticity ( $\omega_z = \partial v/\partial x - \partial u/\partial y$ ) contours. Care should be taken to interpret the vortex based on the vorticity distribution, since concentrated vorticity is an indicator of both vortices and shear layers. According to Adrian et al. [1], swirling strength ( $\lambda_{ci}$ ) can be used to differentiate swirl motion around an axis normal to the 2D measured plane from rotation by a shear layer. Therefore, the swirling strength contours are also overlaid on this plot by red lines, of which the peak location is regarded as the vortex core. The sequence is taken at nine equally separated time intervals of  $1/200$  s from 1,265 consecutive instantaneous velocity fields. The convective time scale ( $T_c = c/U_0$ ) is used for non-dimensionalization, which works out as  $0.74$  s at  $Re = 60,000$ . The FOV starts at  $x = 76.3$  mm from the airfoil leading edge, around  $4.1$  mm ahead the transition onset.

Initially, an oval-shaped vortex is apparent in the middle of the graph at  $t = t_0$ , with the vortex core at  $x/c = 0.45$

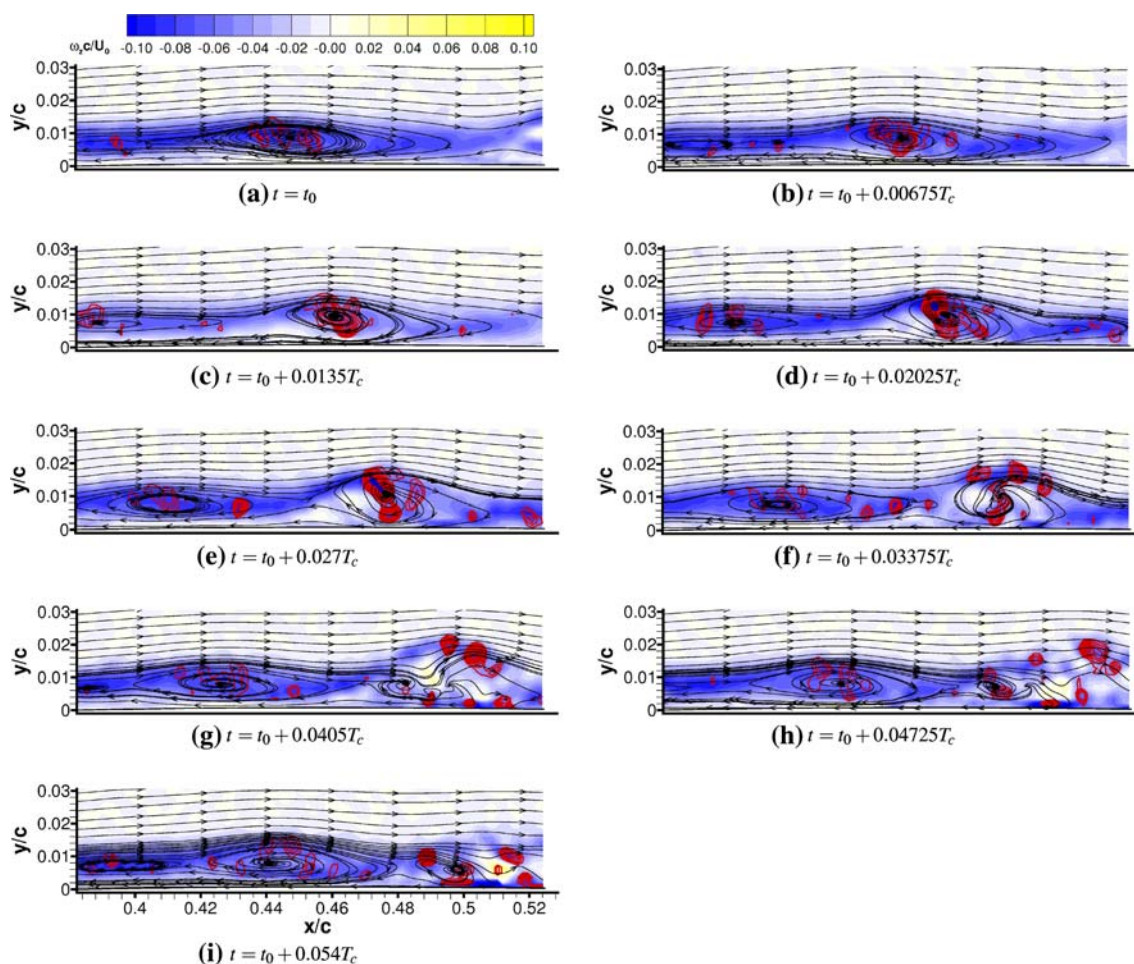


**Fig. 6** Normalized span-wise vorticity ( $\omega_z c/U_0$ ) contours in the single stream-wise wall-normal plane and the streamlines correspond to the instantaneous velocity field ( $u - 0.6U_0$ ,  $v$ ) at  $Re = 60,000$ . The swirling strength ( $\lambda_{ci}$ ) is illustrated by red lines



and  $y/c = 0.0085$ . Then the vortex travels downward and lifts up slightly at  $t = t_0 + 0.00675T_c$ , indicated by the rising trend of the streamlines. The swirling strength contours become accumulated, suggesting the vortex strength is increasing. At the next instant ( $t = t_0 + 0.0135T_c$ ) the vortex lifts up and moves downstream further, with the vortex core at  $x/c = 0.46$  and  $y/c = 0.009$ . It can be seen that another peak of swirling strength shows up at the leftmost side of the FOV, which means the second vortex is coming into vision. Subsequently, the first vortex stretches considerably in both the wall-normal and stream-wise directions, showing a more rounded shape at  $t = t_0 + 0.027T_c$ . The swirling strength of this vortex reaches its maximum in the entire sequence. Also the second vortex fully shows up, with the vortex core at  $x/c = 0.41$  and  $y/c = 0.0075$ . The first vortex starts to break down at  $t = t_0 + 0.03375T_c$ , accordingly, the swirling strength contours become dispersed around the vortex. The dispersed pattern keeps on in the following frames. The second vortex core shifts to  $x/c = 0.42$  and  $y/c = 0.0075$  at the same time. At the last instant ( $t = t_0 + 0.054T_c$ ) of this sequence the first vortex loses most of its strength, only with the remnant of scattered swirling strength contours. The second vortex is fully developed into an oval shape, quite similar to the first primary vortex at  $t = t_0$ .

We applied FFT to a time history (1.265 s) of the fluctuating stream-wise and vertical velocity component  $u'/U_0$  and  $v'/U_0$  (at  $x/c = 0.385$ ,  $0.42$ ,  $0.45$  and  $y/c = 0.0033$ ) from the data in the stream-wise wall-normal plane to estimate the vortex shedding frequency. It turns out that the dominant frequency is 10.7 Hz as shown in Fig. 7. The frequency of 1.2 Hz is considered to associate to a low

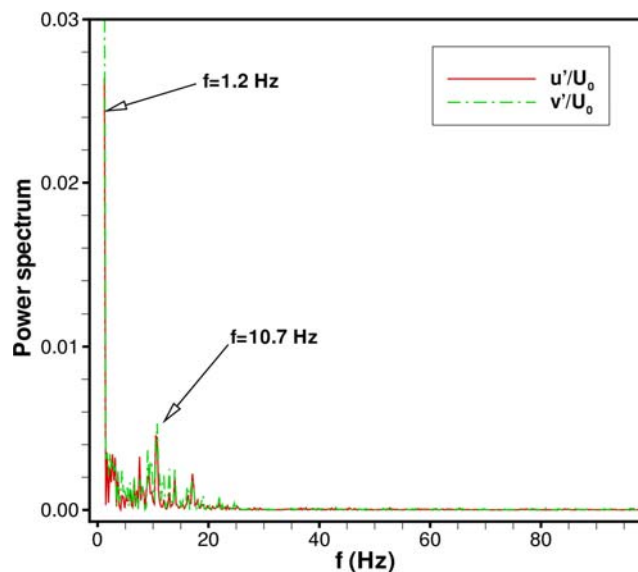


**Fig. 7** Power spectrum of fluctuating stream-wise and vertical velocity component  $u'$  and  $v'$  at  $x/c = 0.385$  and  $y/c = 0.0033$  at  $Re = 60,000$

frequency flapping of the LSB. This result is consistent with the estimation reported in [13] using the time-resolved PIV data for the same airfoil at angle of attack of 4 degrees at  $Re = 60,000$ . Previous research regarding the LSB formed in a very low-disturbance environment [28, 31], generally agree that the primary instability mechanism in transition is initially T–S mode and it can maintain dominance up to the separated flow region. Thereafter K–H instability becomes the leading mechanism in the rear part of LSB.

Figure 8 shows a selective time sequence of iso-surfaces of the normalized span-wise vorticity ( $\omega_z c/U_0$ ) of the scanning volume in the stream-wise wall-normal direction. The physical time interval between two frames is 0.01 s, corresponding to the duration of a full volume scan cycle. For clear visibility only iso-surfaces of normalized span-wise vorticity  $\omega_z = \pm 0.07$ ,  $0.15$  and  $0.22$  are shown. One can observe a slight “bump” in the middle of the FOV at the beginning ( $t = t_0$ ), which is in fact the rising separated shear layer. The laminar boundary layer is subjected to the T–S instability, and the instability waves grow and vorticity sheets are rolling up. In the following instants this separated shear layer grows rapidly and spreads to the downstream. At  $t = t_0 + 0.054T_c$  roll up of the separated shear layer seems to hit its peak, while there appears another “bump” upstream. At the last instant the span-wise vorticity shows a chaotic state, indicating vortex break down. This sequence is the extended presentation of the vortex shedding in a volume from a single plane. Well-organized large vortices, formed in the separated shear layer owing to linear instability, roll up and shed downstream, and then split into a number of small structures and break down to turbulence. Because the instantaneous flow field is highly unsteady in transition, especially near the reattachment point, not only the vertical height but the length of the LSB are time dependent. Also, it should be kept in mind that the measurement planes of a scanning volume are fixed, whereas the vortex structure undertakes somehow oblique movement along traveling downstream, as will be shown in Fig. 11. Therefore, the slice of the vortex shape and size will vary depending on the specific instant it is captured and the position where it is cut.

This whole sequence resolves the physical process of vortex shedding in transition. Once a vortex is formed due to the separated shear layer roll-up, it then develops gradually and propagates downstream until it breaks down into small scale vortical structures at about the reattachment point, which are convecting downstream in the reattached turbulent boundary layer. Observation of the sequence clearly shows an overall flapping motion of the separated shear layer. Accordingly, the LSB is vertically oscillated and its height varies periodically. The fluctuation in the height of the LSB also indicates that outer

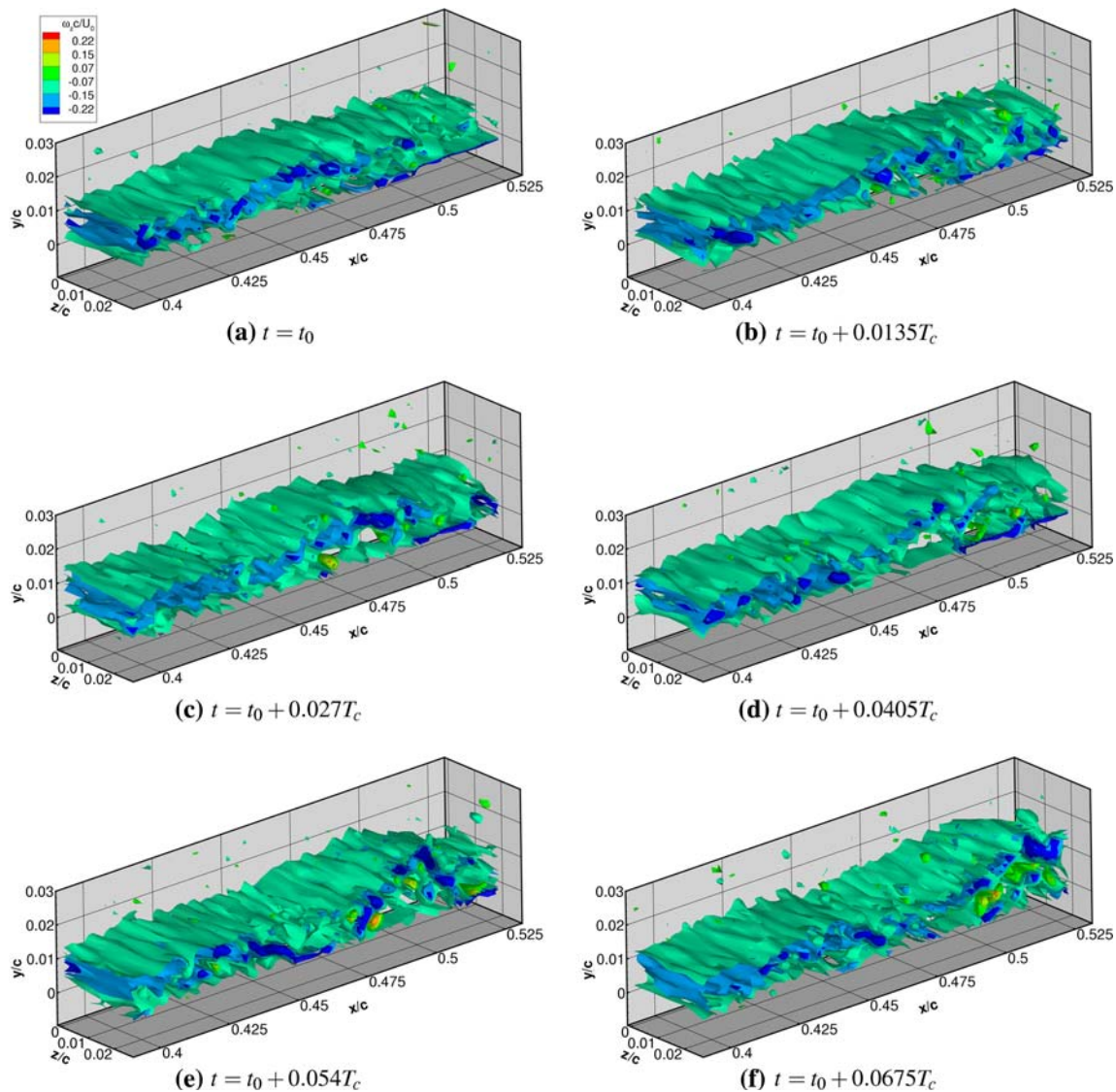


**Fig. 8** Selective time sequence of iso-surfaces of the normalized span-wise vorticity ( $\omega_z c/U_0$ ) of the scanning volume in the stream-wise wall-normal direction at  $Re = 60,000$

fluid is continuously entrained to ensure the vortex shedding process. The phenomenon observed here is similar to the unsteady computational case in [25], and vortex evolution near the reattachment region reported by [8].

The roll-up and breakdown of the vortices from the separated shear layer is typical of laminar-turbulent transition dominated by K–H instability, as mentioned in [29, 32] among others. This suggests that the K–H instability would be the primary instability mechanism after transition in the LSB. In addition, the vortical pattern looks like a “cat eye”, which is regarded as the characteristic of K–H instability [30]. This is not surprising since the K–H instability becomes dominant in the separated flow region, taking place of the primary T–S instability mechanism in the early stage of the transition upstream the separation.

### 3.1.3 Three-dimensional vortex structures

Figure 9 is an example of an instantaneous velocity field of a scanning volume in the stream-wise wall-normal direction at  $Re = 60,000$ . The scanned planes are at  $z = 0, 1.3, 2.6, 3.9, 5.2$  mm ( $z/c = 0, 0.0065, 0.013, 0.0195, 0.026$ ). The normalized stream-wise velocity magnitude is color coded. This figure is zoomed in the  $z$  direction for clear visibility. Though good correlation of the flow structure in the scanning volume is obvious, visible variation of the flow in the scanning volume depth can be detected. For a close observation, the streamlines corresponding to the instantaneous velocity field ( $u - 0.6U_0, v$ ) in each plane (in Fig. 9) are shown in Fig. 10. Vortex centers are identified by considering both the streamlines and the swirling

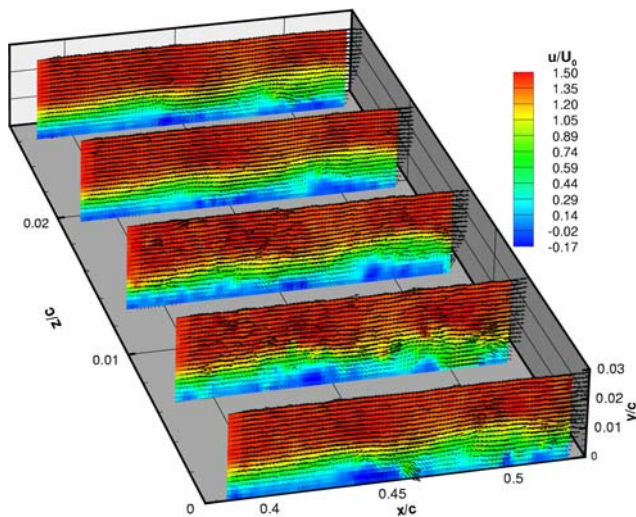


**Fig. 9** Example of an instantaneous velocity field of a scanning volume in the stream-wise wall-normal direction at  $Re = 60,000$

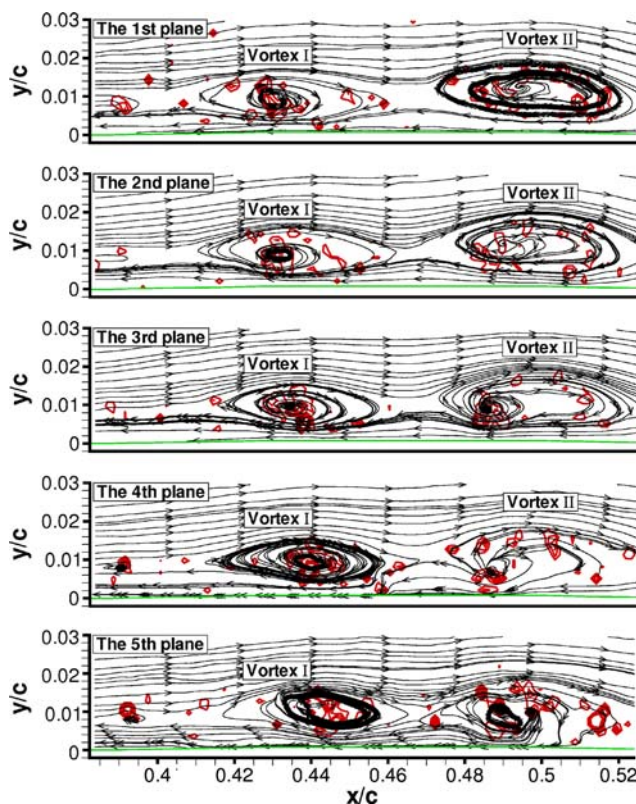


**Fig. 10** Streamline distribution correspond to the instantaneous velocity field ( $u = 0.6U_0$ ,  $v$ ) in each plane of the scanned volume shown in Fig. 9. Swirling strength ( $\lambda_{ci}$ ) indicated by the red lines are overlaid to show the vortex center. The airfoil surface is marked with the green line

strength distribution. It can be seen that the center of vortex I gradually moves downstream from the first plane to the fifth plane. However, the center of vortex II seems to migrate upstream from the first plane to the fourth plane. It

is noticed that the structure of vortex II in the fifth plane seem to have a poor correlation with that in the other four planes. Probably this flow structure is coming from the third vortex. This observation reveals that the overall vortex structure in transition differ in the span-wise direction, indicative of significant 3D structures of the LSB. Note that this scan is just chosen as a typical but not general example to show the 3D spatial vortex structure in the laminar-turbulent transition. Owing to the limited size of FOV in Figs. 9 and 10, it is hard to comment on the flow span-wise uniformity. However, more information can be found in the scanning surface-parallel planes. Later Fig. 12a indicates that beyond  $y/c = 0.015$  the flow upstream of transition is very uniform in the span-wise direction. The stream-wise velocity contours in the lowest two scanning planes ( $y/c = 0.005$  and  $0.01$ ) in the form of intermittent streaks evidenced the span-wise non-uniformity of the flow in the near wall region.

An exemplary instantaneous flow field measured in the single surface-parallel plane, approximately  $0.7\text{ mm}$  ( $y/c = 0.0035$ ) away from the airfoil surface at  $x/c = 0.382$  is shown in Fig. 11. Note that the spacing between the illuminated plane and the airfoil surface varies slightly in the stream-wise direction because of the airfoil surface curvature. This should be applied as well to all the measurements in the so-called surface-parallel planes. The measurement area is about  $92.3\text{ mm} \times 68.4\text{ mm}$ , which is large enough to cover the laminar-turbulent transition and the reattachment region of the LSB and is able to provide an overview of the flow structures. The low velocity region is present between  $x/c = 0.375\text{--}0.525$ , followed by the velocity recovery area. From the aforementioned results in the stream-wise wall-normal planes, this low velocity area corresponds to the LSB. Specifically, the low velocity region with a roughly triangular shape could be the track of the vortical structure formed in transition. The corresponding wall-normal vorticity ( $\omega_y$ ) contours in Fig. 11b depicts two arms of this triangular structure, marked by the black circle. This can be considered as a dominant flow structure; however, the wall-normal vorticity and the swirling strength intensity are not necessarily symmetric for the two arms. With a few such structures in transition, there shows a more or less “sinuous” interface of low velocity and the velocity recovery regions. This vortex structure is quite similar to observation of a LSB on a flat plate made by Lang et al. [23], who reported the occurrence of counter-rotating vortex pairs in the laminar-turbulence transition. In the reattached turbulent boundary layer high and low velocity streaks are distributed interactively in the span-wise direction. As a result, examination of the whole time sequence reveals that these streaks move in a somehow oblique means. It can be also seen that, the vortices formed in the vicinity of the

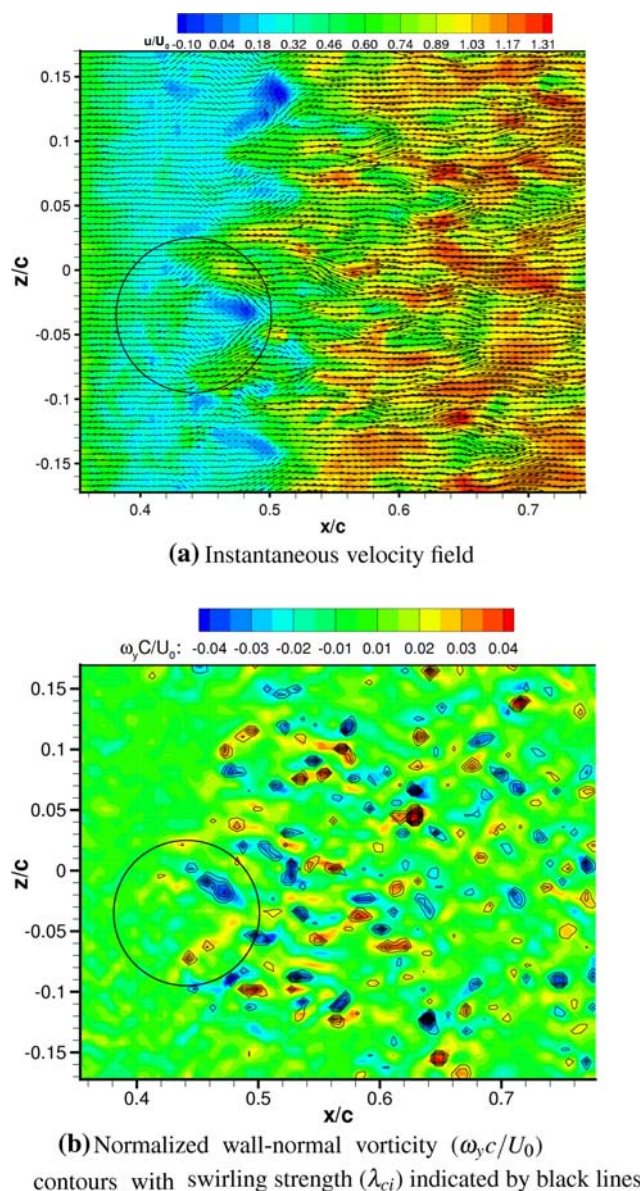


**Fig. 11** Instantaneous flow field in the airfoil surface-parallel plane ( $y/c = 0.0035$ ), the FOV covers  $x/c = 0.35$ – $0.82$  in the middle of airfoil span at  $Re = 60,000$

reattachment point propagate downstream, and retain their identity in a long distance in the turbulent boundary layer. For instance, not until  $x/c = 0.65$  the intensity of both vorticity and swirling strength have not decreased significantly compared with their peak values.

Figure 12 shows the instantaneous stream-wise velocity distribution observed in the two surface-parallel scanning volumes, with the airfoil surface at  $y = 0$ . As one can see in Fig. 12a, the stream-wise velocity magnitude contours are very uniform at the beginning of the FOV, which is assumed as the 2D laminar flow regime. Generally, the stream-wise velocity increases away from the airfoil surface. In the scanned plane closest to the airfoil surface at

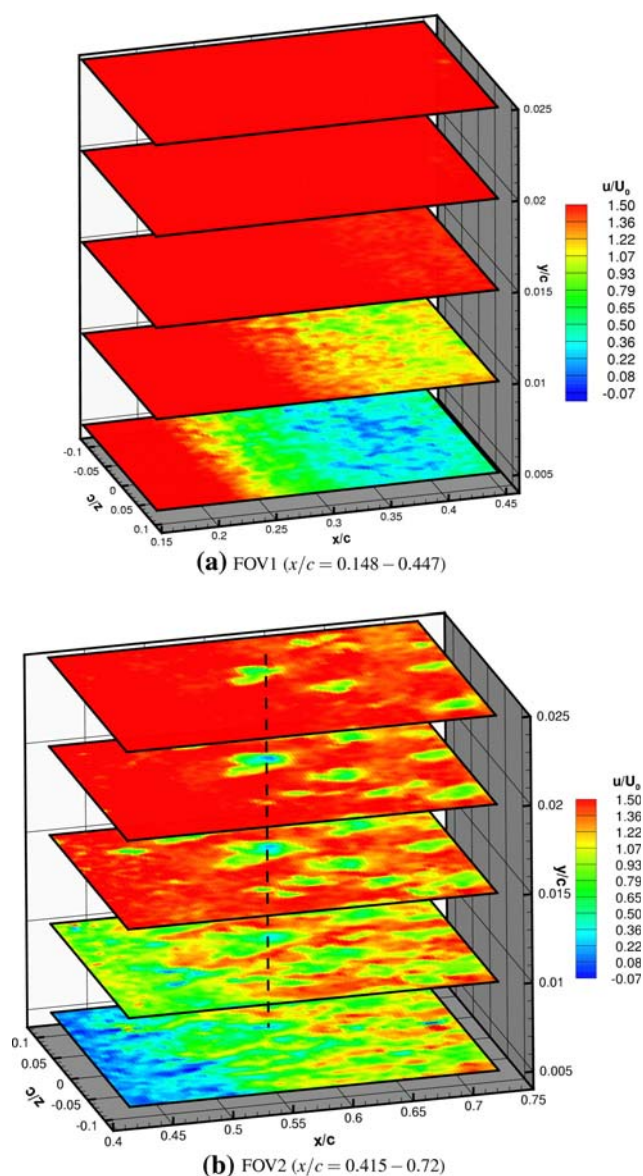


**Fig. 12** Typical instantaneous velocity fields of the scanning volume in the surface-parallel planes at  $Re = 60,000$ . The airfoil surface is located at  $y = 0$  at  $x/c = 0.382$ . Flow is from left to right

$y/c = 0.005$ , the stream-wise velocity defect occurs at approximately  $x/c = 0.21$ , followed by separated flow downstream. This separation point drifts downward in other planes with increasing distance from the airfoil surface. Reversed flow can be seen from  $x/c = 0.323$  in the scanned plane at  $y/c = 0.01$  till the end of this FOV. However, nearly no reversed flow is resolved in other scanned planes at this specified instant. Compared with the time mean velocity distribution discussed in Sect. 3.1.1, the current result shows a good consistency.

The scanned planes in the second FOV are located at  $y/c = 0.005, 0.01, 0.015, 0.02$  and  $0.025$  with the airfoil surface being about  $y = 0$ . As can be seen from the

previous results, this FOV in Fig. 12b covers the laminar-turbulent transition and the reattached turbulent boundary layer. The flow structure in the scanned plane closest to the airfoil surface is similar to that shown in Fig. 11. In other planes the stream-wise velocity magnitude contours display diverse irregular stripes and streaks, indicating the inherent turbulent 3D features. Compared with the numerous flow structures presented in the near-wall plane, fewer structures are apparent in the planes moving away from the wall, hence they can be observed more easily. Inspection of the entire scanning volume shows a strong spatial correlation of the flow structures. For instance, the local region with low stream-wise velocity marked by the black dashed line is very noticeable in the upper four scanned planes, indicative of the same vortex structure throughout the entire scanning volume. Apparently the second FOV is more interesting for exploring the vortical structure evolution than the first one.

For further studying the three-dimensional motion and disturbance growth, Fig. 13 shows the peak RMS values of three velocity components on the suction side of the airfoil SD7003 at  $Re = 60,000$  extracted from the velocity fields in the stream-wise wall-normal plane and in the surface-parallel plane ( $y/c = 0.0035$ ).  $u'/U_0$  is about 0.06 at  $x/c = 0.36$  and undergoes a slow increase to 0.08 till  $x/c = 0.40$ . Downstream the fluctuation  $u'/U_0$  grows violently in the range of  $x/c = 0.40–0.51$  and reaches the maximum of 0.26 at around  $x/c = 0.51$  where re-attachment takes place. Similarly, peak values of  $v'/U_0$  and  $w'/U_0$  rise sharply at  $x/c = 0.38–0.51$  up to their maximums of 0.13 and 0.17, respectively. It is evident that the maximum fluctuations occur just before the mean reattachment point;

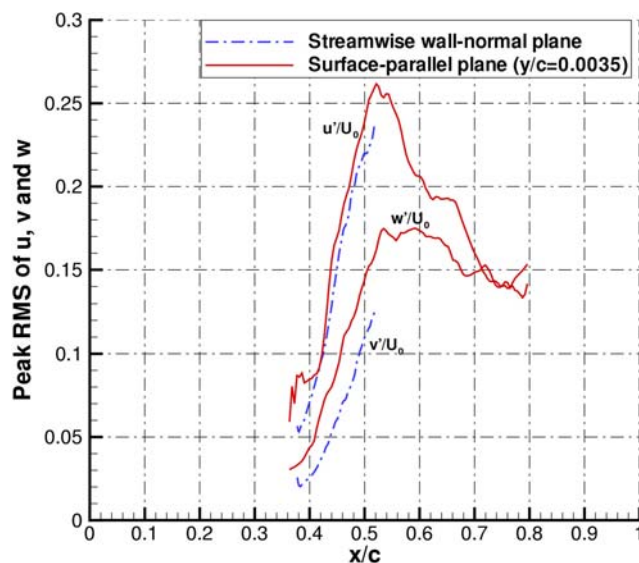


**Fig. 13** Peak RMS of three velocity components on the suction side of SD7003 at  $Re = 60,000$

afterward the disturbance reduces. The significant amplification of the disturbances in the range of  $x/c = 0.4–0.51$  confirms flow transition from laminar to turbulent, and downstream the three-dimensional motion and nonlinear interaction lead to break down to full turbulence. The trend of span-wise velocity component  $w'/U_0$  also reveals that flow starts to display 3D characteristics prior to the transition point ( $x/c = 0.40$ ).

### 3.1.4 Vortex evolution

The scanning volume composed of several surface-parallel planes enables us to observe vortex evolution in the orthogonal view. A sequence of wall-normal vorticity iso-surfaces ( $\omega_y = \pm 0.07$ ) at  $Re = 60,000$  is shown in Fig. 14. The physical time interval between every two graphs of 0.01 s, corresponding to the duration of a scanning cycle, is normalized by the convective time scale of 0.74 s. The graph is zoomed in the  $y$  direction to display the structure with good visibility, which results in elongated vortical structures. The real topology of this vortical structure should look like a sphere rather than an elongated tube. It can be seen that pairs of wall-normal vorticity packets (whether symmetric or not) with positive and negative vorticity values are dominant structures. Back to the discussion in Sect. 3.1.3 these vortices correspond to the “triangular” structures with two arms observed in the near-wall surface-parallel plane. Taking the wall-normal vorticity packets labeled with  $A$  and  $B$  as an example, a typical process of vortex evolution can be detected. Packet  $A$  and  $B$  rise up from the wall at  $t = t_0$  with very small size. In the following instants both vorticity packets grow and travel downstream gradually. During this process there happens vortex stretching, tilting and tearing, which are unavoidable in the turbulent flow full of miscellaneous vortical structures. At  $t = t_0 + 0.054T_c$  they develop fully into the large-scale structures, located in the middle of the observation domain. Until the end of the time span the vorticity packets  $A$  and  $B$  are still clearly visible. No significant deformation in their shape is detected from  $t = t_0 + 0.0675T_c$  to  $t = t_0 + 0.108T_c$ , while vortex reconnection occurs between packet  $A$  and another small vorticity packet coming through the near wall plane at the last three instants of this sequence. Similarly, a pair of vorticity packets labeled with  $D$  and  $E$  shifts downstream from  $t = t_0$  to  $t = t_0 + 0.0675T_c$ . In addition, a group of vorticity packets marked with  $C$  is another interesting example. They are located in the middle of the measurement domain at the beginning of the time span, composing of a few of vorticity packets with various shapes and sizes. Along moving downstream the original compact group becomes dispersed, for instance, starting from  $t = t_0 + 0.0675T_c$ . Interaction within the group  $C$  happens

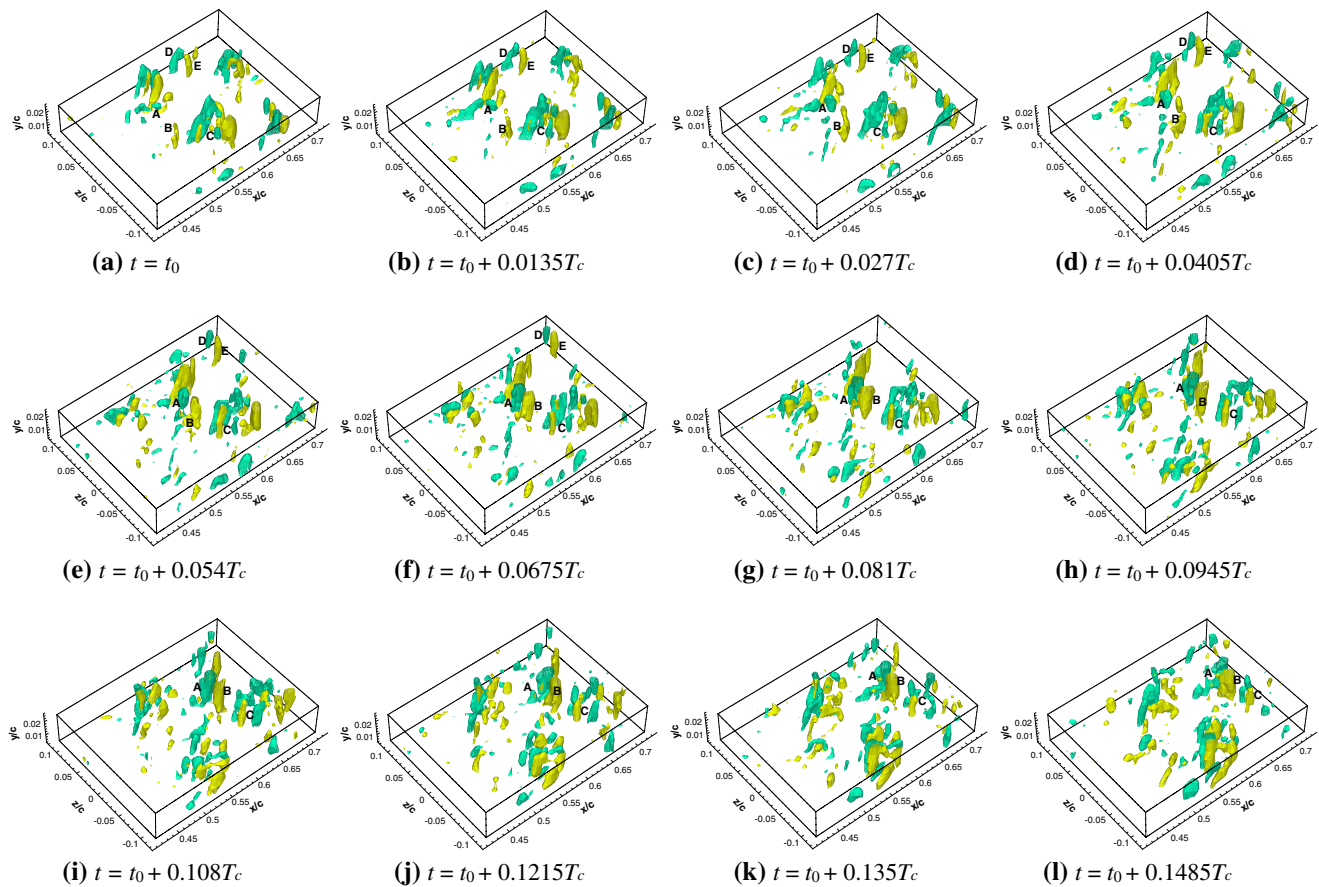


**Fig. 14** Sequence of the normalized wall-normal vorticity contour iso-surfaces ( $\omega_y c/U_0 = \pm 0.07$ ). Yellow and green color indicate positive and negative vorticity value, respectively. The time interval between two graphs is  $0.0135 T_c$ , corresponding to a scanning cycle

as well, including vortex tilting, tearing and redistribution. It can be seen that at  $t = t_0 + 0.1215T_c$  and  $t = t_0 + 0.135T_c$  some vorticity packets in the group C move out of the measurement section, others are still visible. At the last instant only relics of group C remain in the FOV. By overlapping the vorticity iso-surfaces in this time sequence (see Fig. 15), vortex evolution in the turbulent boundary layer can be clearly identified.

From behavior of the vorticity packets in this time span, two outstanding features are summarized as following: Firstly, vorticity packets are continuously generated from the airfoil surface even prior to the transition onset ( $x/c = 0.40$ ) and then developed and transported downstream. It is understandable in that the solid surface is the major source of the vorticity generation in the incompressible flows due to the non-slip wall condition. Secondly, though vortices propagate in the reattached turbulent boundary layer, showing miscellaneous sizes and forms and undergoing complicated vortex interaction, the frequently detected structures are the paired vorticity packets. It could be conjectured that these paired vorticity packets are formed due to the development of 3D motion

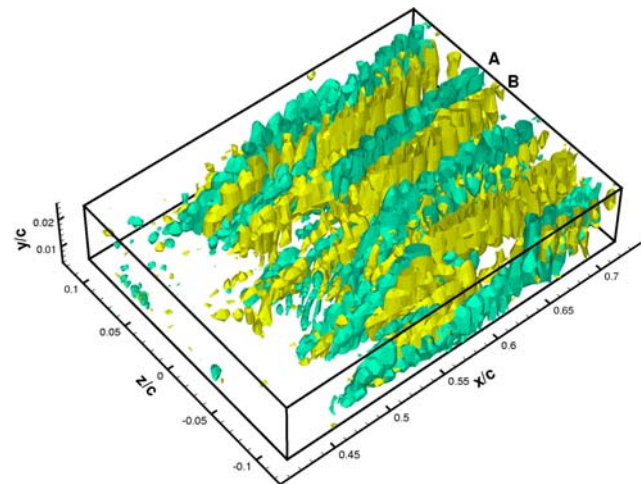


**Fig. 15** Overlapping of the normalized wall-normal vorticity iso-surfaces ( $\omega_y c/U_0 = \pm 0.07$ ) of the selected time sequence in Fig. 14

during the laminar-turbulence transition, after the vortex breakdown in the vicinity of the reattachment position. And they transport low velocity fluid away from the near airfoil surface region. It is also noticeable that the well-organized

structures can be identified from the random turbulent surroundings, though mutual interaction among them occurs all the time. Since the measurement from two orthogonal views are not simultaneous, no determined comments can be made on the relationship between the span-wise and wall-normal vorticity.

### 3.2 Flow structures of LSB at $Re = 20,000$

The purpose of this measurement case is to explore the structure of LSB at a lower Reynolds number and the difference resulted from Reynolds number by comparing with the results obtained at  $Re = 60,000$ . The turbulence level of the employed water channel will be a little higher at  $Re = 20,000$  but still comparable to that at  $Re = 60,000$ . Burgmann et al. [9] reported the spatial and temporal structure of the separation bubble on the SD7003 airfoil at the angle of attack  $\alpha = 4\text{--}6^\circ$  and  $Re = 20,000$ . It would be interesting to compare some of the features exhibited in the present observation with some of their results.

#### 3.2.1 In the stream-wise wall-normal planes

For the scanning PIV measurements in the stream-wise wall-normal direction, the light-sheets were adjusted to cover the area of  $x/c = 0.65\text{--}0.79$  and  $y/c = 0\text{--}0.03$  and to capture particle images with acceptable illumination. Figure 16 demonstrates an example of the instantaneous flow field of a scanning volume at  $Re = 20,000$ . Scanned planes are positioned at  $z/c = 0, 0.0065, 0.013, 0.0195, 0.026$ , respectively. Color coded in Fig. 16b is the normalized stream-wise velocity component  $u/U_0$ . As shown by the velocity vectors distributed every other column, a salient large vortex is apparent in the rear half of each scanned plane over the entire volume. The vortex center can be identified with certain in the planes at  $z/c = 0.013, 0.0195$  and  $0.026$ , while it is out of view in the plane at  $z = 0$ . The trend of reversed flow near the wall suggests that the vortex center migrates away from the wall from  $z/c = 0.026$  to  $z = 0$ . The deviation of the vortex center and variation of the velocity vector fields in the scanning volume evidence the highly 3D turbulent flow. Compared with the mean flow at  $Re = 60,000$  (in Fig. 5) the scale of vortex structure is dramatically huge. Using a scanning light sheet of only 6 mm high is obviously not able to resolve the full flow structures at  $Re = 20,000$ . Figure 17 shows two volumetric presentations of the instantaneous flow in the stream-wise wall-normal planes. A counter-clockwise vortex is shown in the first example, while only half of a huge clock-wise vortex is visible in the second example.

With the purpose of visualizing the full vortex structure, the light-sheet was intentionally enlarged to cover  $y/$

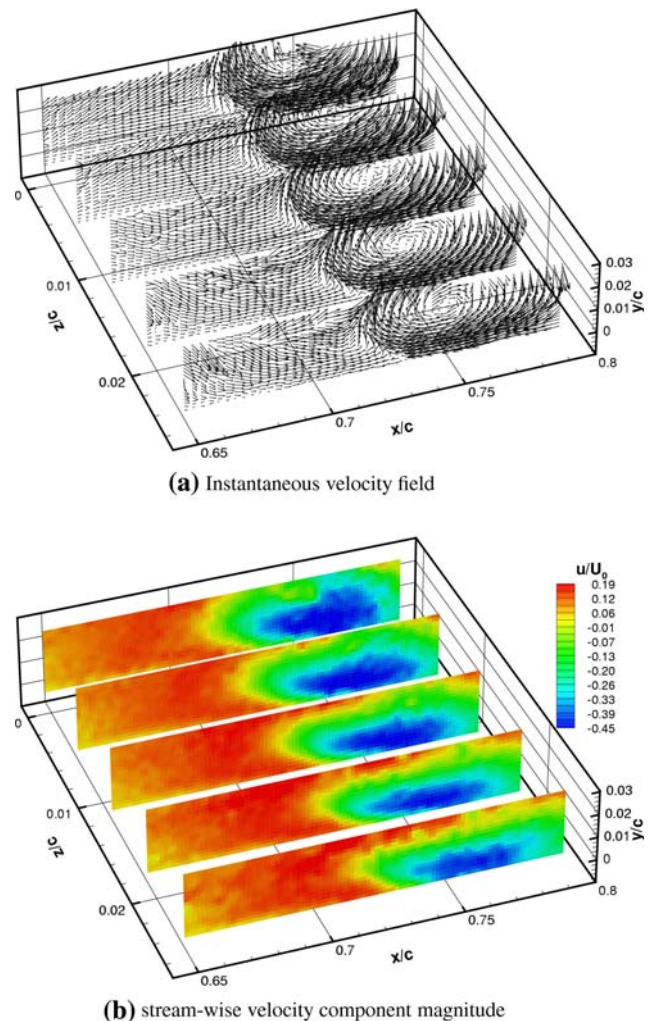


**Fig. 16** Example of instantaneous velocity vector fields in the stream-wise wall-normal planes at  $Re = 20,000$ . The airfoil surface locates at  $y = 0$ . Measurement planes are at  $z/c = 0, 0.0065, 0.013, 0.0195, 0.026$ . velocity vectors are shown every other column in the stream-wise direction. Color coded is the stream-wise velocity component magnitude

$c = 0\text{--}0.0525$  in the single stream-wise wall-normal plane at mid-span of the airfoil. The instantaneous streamlines in a sequence are shown in Fig. 18. The physical time interval of 0.1 s is normalized by the convective time scale of 2.22 s at  $Re = 20,000$ . The flow is characterized by co-existing large and small vortices, distinctly different structures from those at  $Re = 60,000$ . The largest vortex observed in this sequence is barely covered by the enlarged light-sheet. Taking into account the high level of unsteadiness, the instantaneous height of the separation bubble is estimated to be larger than  $y/c = 0.0525$ . The mean flow field at  $Re = 60,000$  in Fig. 5 shows that the separation bubble is restricted within  $y/c = 0.015$ . This result also indicates that the boundary layer thickness is very wide in the present measurement section at

$Re = 20,000$ . In addition, the dominant vortex shedding frequency is estimated to be around 2.2 Hz at  $Re = 20,000$ .

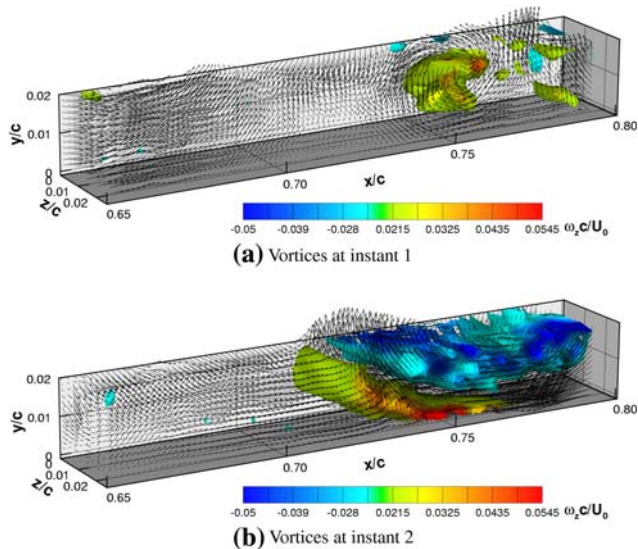


**Fig. 17** Instantaneous velocity fields of two scanning volumes (stream-wise wall-normal planes) at  $Re = 20,000$ , with iso-surfaces of the span-wise vorticity indicated by *color flood*

### 3.2.2 In the surface-parallel planes

As in the case of  $Re = 60,000$ , flow at  $Re = 20,000$  is also observed in the surface-parallel planes (Fig. 19). In the first measurement domain, normalized stream-wise velocity gradually increases moving away from the airfoil surface with a trend similar to that at  $Re = 60,000$ . The measurement of the second zone is remarkably larger than that at  $Re = 60,000$ , in that we extended the scanning volume depth from 4 to 8 mm based on the observation of large scale vortices above mentioned. Correspondingly, the scanned planes are located at  $y/c = 0.005, 0.015, 0.025, 0.035$  and  $0.045$  with the airfoil surface at  $y = 0$ . Figure 19b shows the normalized instantaneous stream-wise velocity contours in a scanning volume of the second FOV. The correlation among the flow structures in each plane can be identified by the local low velocity fluid region marked by the dashed line. The flow separation is estimated directly from the instantaneous velocity distribution in the surface-closest plane of the first FOV, see Fig. 19c. The stream-wise velocity becomes negative at approximately  $x/c = 0.28$ . However, the real separation point would be further upstream of this estimated value since this plane is located about 1 mm ( $y/c = 0.005$ ) away from the airfoil surface.

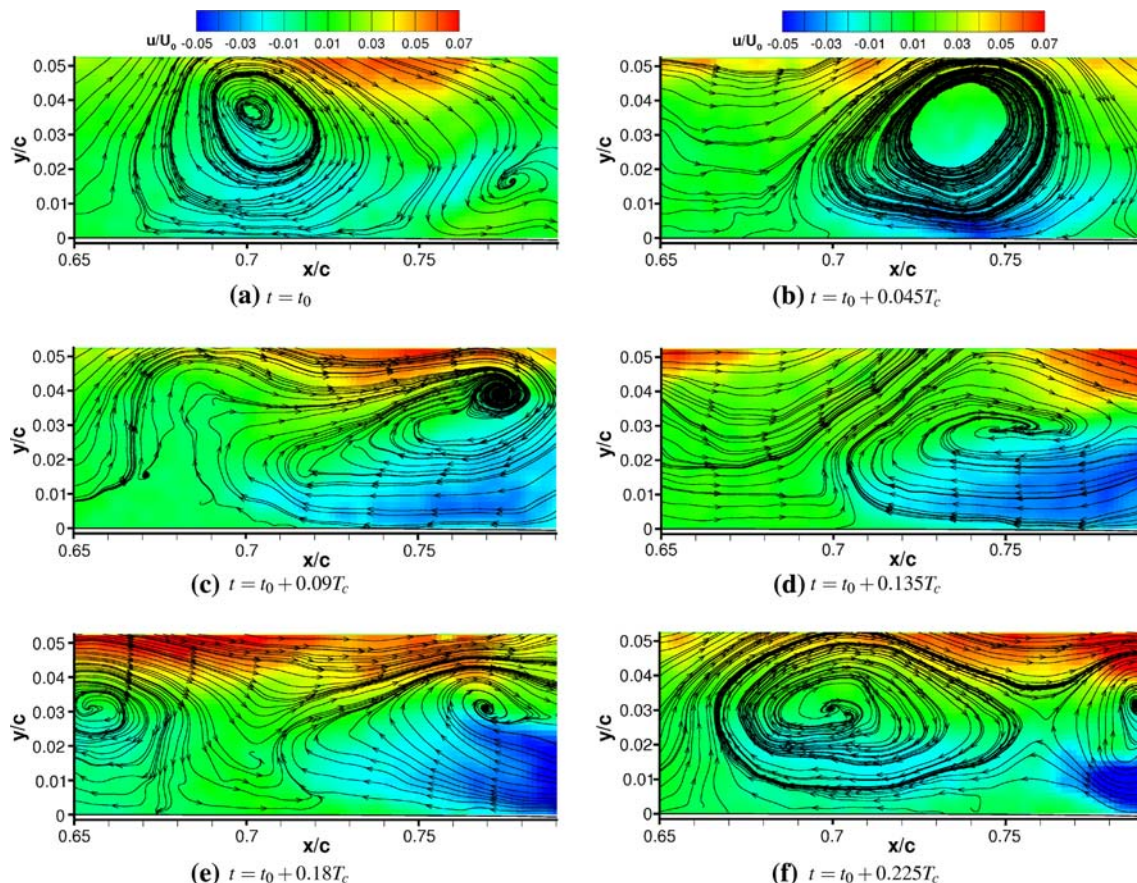


**Fig. 18** Instantaneous streamlines in a selective sequence with the normalized time interval of  $0.045 T_c$  at  $Re = 20,000$



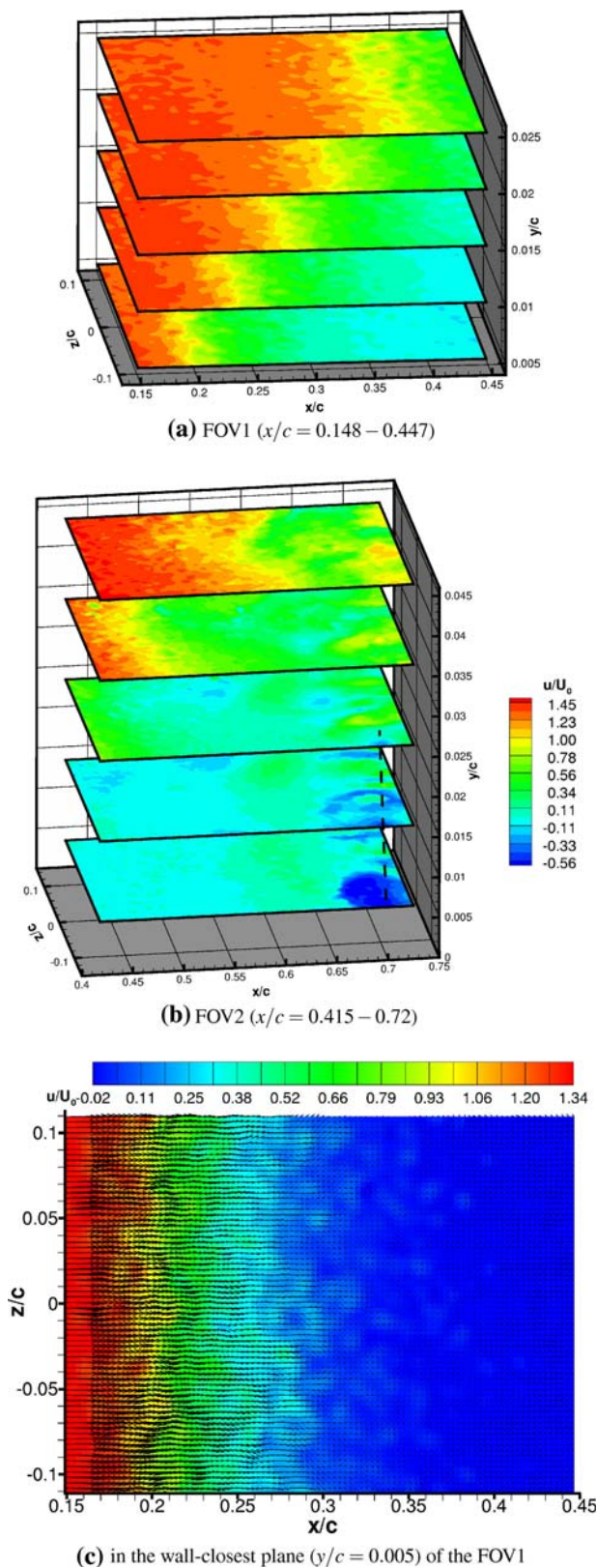


**Fig. 19** Instantaneous stream-wise velocity magnitude distribution of two scanning volumes (*surface-parallel planes*) at  $Re = 20,000$ , with the airfoil surface at  $y = 0$

The volumetric presentation of the flow structure in the surface-parallel planes is shown in Fig. 20. Both the normalized stream-wise velocity contours and the vector field indicate the large low velocity region in the most part of the measurement domain near the wall. Apparently this low velocity region expands in the wall-normal direction with flow moving downstream. In the end right corner of the test zone there appears a strong local reversed flow. From the iso-surfaces of the wall-normal vorticity, we can see that the vortical structures accumulate in the rear part behind  $x/c = 0.6$ . The vorticity distribution over the entire scanning volume confirms again the huge vortical structures at  $Re = 20,000$ . Combining our observation in two orthogonal views, we can deduce that the flow separates upstream of  $x/c = 0.28$  and reattaches, if at all, downstream of  $x/c = 0.79$ . It is also possible that what we observed is a portion of an open LSB. This could happen if the transition is relatively slow and the adverse pressure gradient is strong, so the turbulent momentum is not sufficient to make the separated shear layer reach the airfoil surface and close the bubble. Finally a huge separation flow may appear and even extend to the trailing edge.

Burgmann et al. [9] measured a volume of  $60 \times 40 \times 5 \text{ mm}^3$  covering  $x/c = 0.6-0.9$  in the stream-wise direction at the same angle of attack and Reynolds number in a water tunnel with the turbulence level of 1.5%. They depicted a primary vortex (C-shape vortex) mainly formed between  $x/c = 0.6-0.75$  and secondary vortices formed downstream, such as the so-called “screwdriver” vortex. In their results the vortical structures of a closed LSB were fully resolved within 5 mm ( $y/c = 0.025$ ) above the airfoil surface, which is much smaller than the dimension of vortices observed in the present study. Rist [27] remarked that the separation, transition and re-attachment were subject to subtle changes in the stream-wise pressure gradient, which means the LSB is very sensitive to the ambient background disturbance, especially the turbulence level of the water tunnel. The difference in the turbulence intensity of the water facility is expected to play a significant role in the dynamic vortical behavior and vortex evolution. Furthermore, the large separation observed at  $Re = 20,000$  is an indicator of hysteresis effect, that is, the airfoil aerodynamic characteristics and associated flow phenomena become history dependent. The statements suggest extreme care be taken when comparing results from different experiments or numerical simulation. However, the real reasons resulting in the large difference in the vortical structures need to be explored through further study.

#### 4 Conclusion

The objective of this study is to investigate the LSB formed on the suction side of a SD7003 airfoil at the angle of

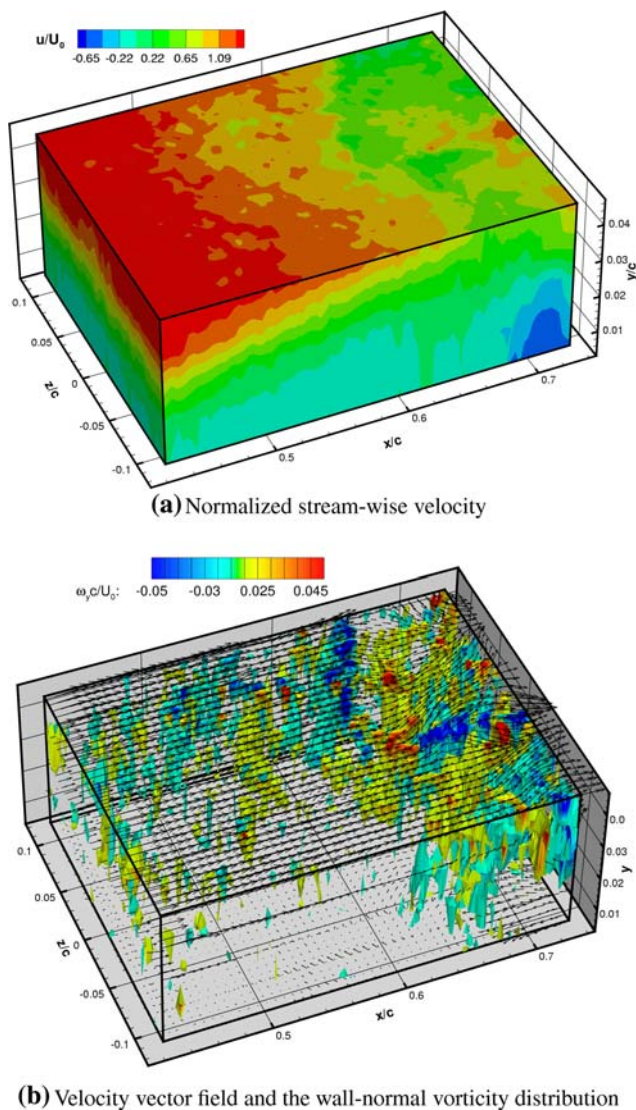


**Fig. 20** Flow structure in a surface-parallel scanning volume at  $Re = 20,000$

attack of 4 degrees at low Reynolds numbers. In view of inherent unsteadiness and 3D structure of the flow, quasi-3D PIV measurements were performed with the scanning PIV technique. Observation was made from two orthogonal views, one in the stream-wise wall-normal direction, the other in the airfoil surface-parallel direction.

For the case at  $Re = 60,000$  the transition onset is at 40% chord length and reattachment locates at 51% chord length, estimated via the mean flow field. The vortex shedding process is presented with the span-wise vorticity not only in the single plane at the middle span but the scanning volume in the stream-wise wall-normal direction. This measurement is done in a relatively small domain, to ensure a high spatial resolution of the small LSB. Furthermore, the measurement from the surface-parallel planes reveals vortical structures in an extended region, covering

the laminar-turbulent transition and reattached turbulent boundary layer. It can be seen very clearly that the vortices form in the vicinity of the reattachment point then propagate downstream. Even in a long distance these vortices keep their identity in the turbulent boundary layer. Right after the reattachment low-speed streaks can also be observed in the near-wall region which are typical coherent flow structures in turbulent boundary-layer flows [20, 21]. The flow at  $Re = 20,000$  presents an early separation, followed by a large low velocity region. Occurrence of dramatically huge vortical structures is the main feature at the measurement domain. The LSB increases in size with decreasing Reynolds number and the reattachment region would be getting closer and closer to the trailing edge. This has a strong effect on the flow structures in both the laminar-turbulent transition and the reattachment region since a full turbulent flow region behind the reattachment line would be replaced by the wake of the airfoil.

It has been mentioned that the scanning PIV technique employed here is a quasi-3D measurement technique which can obtain two velocity components in the discrete slices of a scanning volume. Therefore the interpretation of results is based on 2D variable distribution without the third velocity component. Additional efforts are worthwhile to extract all three velocity components to resolve the real 3D flow, with stereoscopic imaging setup as done by Brücker [6] and Burgmann et al. [9] for instance, or by using newly developed tomographic PIV technique [14]. The strategy of applying scanning PIV method to a given tested flow is always a compromise since both the temporal and spatial resolution should be carefully considered to get at least a good approximation of the real instantaneous flow field. In this sense, the requirement of the working frequency of the light source and the scanning device, as well as the energy output of the light source is crucial. In the present study the scanning volume depth is constrained to be around 5 mm to ensure the spatial resolution, which obstacles the observation of the full vortex structure in LSB. However, this problem can be partially solved with a high-power high-frequency laser to provide enough illumination to the seeding particles.

**Acknowledgments** This research has been supported by the German Research Foundation (DFG) in the priority program 1147 “Bildgebende Messverfahren für die Strömungsanalyse”.

## References

1. Adrian RJ, Christensen KT, Liu XF (2000) Analysis and interpretation of instantaneous turbulent velocity fields. *Exp Fluids* 29:275–290
2. Alam M, Sandham ND (2000) Direct numerical simulation of “short” laminar separation bubbles with turbulent reattachment. *J Fluid Mech* 410:1–28

3. Brücker Ch, Althaus W (1992) Study of vortex breakdown by particle tracking velocimetry (PTV) Part I: bubble-type vortex breakdown. *Exp Fluids* 13:339–349
4. Brücker Ch (1995) Digital-particle-image-velocimetry (DPIV) in a scanning light-sheet: 3D starting flow around a short cylinder. *Exp Fluids* 19:255–263
5. Brücker Ch (1997a) 3D scanning PIV applied to an air flow in a motored engine using digital high-speed video. *Meas Sci Technol* 8:1480–1492
6. Brücker Ch (1997b) Study of the three-dimensional flow in a T-junction using a dual-scanning method for three-dimensional scanning-particle-image velocimetry (3-D SPIV). *Exp Thermal Fluid Sci* 14:35–44
7. Brücker Ch, Burgmann S, Schröder W (2005) Scanning PIV measurements of a laminar separation bubble. 2006. In: 6th international symposium on particle image velocimetry. Pasadena, 21–23 Sep, 2005
8. Burgmann S, Schröder W, Brücker Ch (2006a) Volumetric measurement of vortical structures in the reattachment region of a laminar separation bubble using stereo scanning PIV. In: 13th international symposium on applied laser techniques to fluid mechanics
9. Burgmann S, Brücker Ch, Schröder W (2006b) Scanning PIV measurements of a laminar separation bubble. *Exp Fluids* 41:319–326
10. Gaster (1966) The structure and behaviour of laminar separation bubbles. AGARD CP-4, 813–854
11. Eisenbach S, Friedrich R (2008) Large-eddy simulation of flow separation on an airfoil at a high angle of attack and  $Re = 100,000$  using Cartesian grids. *Theor Comput Fluid Dyn* 22:213–225
12. Elsinga GE, Oudheusden BW, van Scarano F (2005) The effect of particle image blur on the correlation map and velocity measurement in PIV. In: Proceedings of the optical engineering and instrumentation, SPIE annual meeting, paper 5880-37. San Diego
13. Hain R, Kähler CJ (2005) Advanced evaluation of time-resolved PIV image sequences. In: 6th international symposium on particle image velocimetry, Pasadena, 21–23 Sep
14. Hain R, Kähler CJ, Michaelis D (2007) Tomographic and time resolved PIV measurements on a finite cylinder mounted on a flat plate. In: 7th international symposium on particle image velocimetry, Roma, 11–14 Sep
15. Häggmark CP, Bakchinov AA, Alfredsson PH (2000) Experiments on a two-dimensional laminar separation bubble. *Philos Trans R Soc Lond A* 358:3193–3205
16. Hori T, Sakakibara J (2004) High-speed scanning stereoscopic PIV for 3D vorticity measurement in liquids. *Meas Sci Technol* 15:1067–1078
17. Horton (1968) Laminar separation bubbles in two- and three-dimensional incompressible flow. Ph.D thesis, University of London
18. Hu H, Yang Z (2008) An experimental study of the laminar flow separation on a low-reynolds-number airfoil. *J Fluids Eng* 130:051101
19. Jones LE, Stanberg RD, Sandham ND (2008) Direct numerical simulations of forced and unforced separation bubbles on an airfoil at incidence. *J Fluid Mech* 602:175–207
20. Kähler CJ (2004) Investigation of the spatio-temporal flow structure in the buffer region of a turbulent boundary layer by means of multiplane stereo PIV. *Exp. Fluids* 36:114–130
21. Kähler CJ (2004) The significance of turbulent eddies for the mixing in boundary layers. In: Meier, Sreenivasan, Heinemann (eds) IUTAM symposium on “one hundred years of boundary layer research”, Solid mechanics and its application, Göttingen, 11–14 Aug 2006, vol 129, Springer, Heidelberg
22. Kelso RM, Delo C (2000) Three-dimensional Imaging. In: Smits AJ, Lim TT (eds) Flow visualization: techniques and examples, vol 10, Imperial College Press, 245–288
23. Lang M, Rist U, Wagner S (2004) Investigations on controlled transition development in a laminar separation bubble by means of LDA and PIV. *Exp Fluids* 36:43–52
24. Ol MV, Hanff E, McAuliffe B, Scholz U, Kähler CJ (2005) Comparison of laminar separation bubble measurements on a low Reynolds number airfoil in three facilities. In: AIAA paper 2005–5149, 35th AIAA fluid dynamics conference and exhibit, Toronto, 6–9 June
25. Pauley LL, Moin P, Reynolds WC (1990) The structure of two-dimensional separation. *J Fluid Mech* 220:397–411
26. Radespiel R, Windte J, Scholz U (2007) Numerical and experimental flow analysis of moving airfoils with laminar separation bubbles. *AIAA J* 45(6):1346–1356
27. Rist U (2002) On instabilities and transition in laminar separation bubbles. In: Proceedings CEAS aerospace aerodynamics research conference, 10–12 June 2002, Cambridge
28. Rist U (2003) Instability and transition mechanisms in laminar separation bubbles, RTO-AVT-VKI lecture series 2004, 24–28 Nov, 2003
29. Spalart PR, Strelets MK (2000) Mechanism of transition and heat transfer in a separation bubble. *J Fluid Mech* 403:329–349
30. Watmuff JH (1999) Evolution of a wave packet into vortex loops in a laminar separation bubble. *J Fluid Mech* 397:119–169
31. Windte J, Radespiel R, Scholz U, Eisfeld B (2004) RANS simulation of the transitional flow around airfoils at low Reynolds Numbers for steady and unsteady onset conditions. ADA442472
32. Yang Z, Voke PR (2001) Large-eddy simulation of boundary-layer separation and transition at a change of surface curvature. *J Fluid Mech* 493:305–333
33. Yuan W, Khalid MC, Windte J, Scholz U, Radespiel R (2005) An investigation of Low-Reynolds-Number flows past airfoils. In: AIAA-2005-4607, 23rd AIAA applied aerodynamics conference, Toronto, 6–9 June